RSC Advances

ROYAL SOCIETY OF CHEMISTRY

www.rsc.org/advances

High gas-sensor and supercapacitor performance of porous Co_3O_4 ultrathin nanosheets

Xiuhua Wang*, Shangwu Yao, Xiaoxiu Wu, Zhijie Shi, Hongxia Sun, Ronghui Que*

Anhui Key Laboratory of Molecule-Based Materials, The Key Laboratory of Functional Molecular Solids, Ministry of Education, College of Chemistry and Materials Science, Anhui Normal University, Wuhu 241000, P. R. China

Fax: +86 553 3869302; Tel: +86 553 3869302; E-mail: xhwang@mail.ahnu.edu.cn

Abstract

Highly porous Co_3O_4 ultrathin porous nanosheets were synthesized by a facile two-step approach, including a hydrothermal technique without any surfactant and followed calcination of precursor. The as-synthesized materials were cubic spinel Co_3O_4 phase according to X-ray diffraction and transmission electron microscopy; and Brunauer-Emmett-Teller measurement showed the surface area was about 97.2 m^2 g^{-1}. Owing to the unique porous ultrathin structural features, the pseudocapacitor capacitance of porous nanosheets was as high as 378 F g^{-1} at a current density of 1 A g^{-1}, and the cycling stability remained about 78.5% after 2000 cycles. In addition, the porous Co_3O_4 ultrathin nanosheets based sensor exhibited good sensitivity and selectivity to ethanol. These results demonstrated that the porous Co_3O_4 ultrathin nanosheets were excellent candidates for electrochemical supercapacitor devices and ideal gas-sensor to ethanol.

Keywords: porous Co_3O_4 ultrathin nanosheets; Electrochemical capacitors; Gas-sensor

1. Introduction

In the past decades, the transition metal oxides have attracted much attention due to their electrical and magnetic properties. Among these materials, Co_3O_4 have been extensively studied due to their excellent properties such as gas-sensing, catalytic and electrochemical ones and potential applications in solid-state sensors and

electrochromic devices.[1-4] Co_3O_4 is an important antiferromagnetic p-type semiconductor.[5] When reduced down to the nanometer scale, Co_3O_4 were found to have interesting electronic, magnetic, and redox properties that are attractive in device applications in energy conversion and storage, magnetic separation, sensor devices and catalysis.[6-10]

Many different techniques have been developed for the preparation of Co_3O_4 nanostructures, such as hydrothermal method,[11] solvothermal method,[12] electrospray deposition,[13] coprecipitation,[14] microemulsions,[15] chemical vapor deposition,[16] sol-gel methods,[17] and so on. And various morphologies and dimensions, including one-dimensional (1D) nanoneedles, nanowires, nanorods, nanobelts and nanotubes, two-dimensional (2D) nanosheets, three-dimensional (3D) nanocubes have been synthesized.[18-21]

It is found that the energy storage and gas-sensor performance of Co_3O_4 strongly depends on its microstructure.[22, 23] Among the reported nanostructures, porous Co_3O_4 nanostructures show better performance in energy storage and gas-sensor due to their fast electron transport and large active interfacial sites owing to the large surface areas. To meet the requirement, many methods have been applied in the synthesis of porous Co_3O_4 nanostructures.

For example, Alshareef et.al synthesized mesoporous Co_3O_4 nanosheet array over flexible carbon paper collectors substrates using electrodeposition method[7]. The group of Tu prepared porous Co_3O_4 nanoflake array grown on nickel foam by a hydrothermal synthesis for pseudocapacitor application.[24] Zhu et.al synthesized mesoporous Co_3O_4 nanoneedle arrays via a facile two-step approach, involving the formation of needle-shaped $Co(CO3)_{0.5}(OH)\cdot 0.11H_2O$ as the precursor and then thermal conversion to mesoporous Co_3O_4.[25] Li and Wang group synthesized Co_3O_4 nanowires growing on the ZnO nanorods through hydrothermal method combined with annealing treatment.[26] Kuang et.al fabricated Co_3O_4 concave nanocubes with high specific surface area by calcining Co-based MOFs.[27] However, pure porous Co_3O_4 ultrathin nanosheets with high surface area have rarely been reported.

The valuable works inspired us to handle the challenges in the synthetic route, such as the using organic surfactants and high calcination temperature of the precursor,

which increasing the environment pollution and high cost.

In our work, we prepared $Co_2CO_3(OH)_2$ precursor via a facile hydrothermal method without any surfactant and porous Co_3O_4 ultrathin nanosheets by subsequent annealing. The as-synthesized porous Co_3O_4 ultrathin nanosheets exhibited good electrochemical performance for supercapacitors and high sensitivity and selectivity to ethanol for gas sensors.

2. Experimental section

2.1 Reagents

Cobaltous acetate ($Co(CH_3COO)_2 \cdot 4H_2O$), urea ($H_2NCONH_2$), ethylene glycol and ethanol were purchased from Sinopharm Chemical Reagent Co., Ltd. All these reagents were of analytical grade and used without further purification. Deionized water was used throughout.

2.2 Synthesis of $Co_2CO_3(OH)_2$ ultrathin nanosheets

The $Co_2CO_3(OH)_2$ ultrathin nanosheets were synthesized via a facile hydrothermal method. In a typical synthesis: 7 mL ethylene glycol was added into 33 mL distilled water under the magnetic string, and then 2 mmol $Co(CH_3COO)_2 \cdot 4H_2O$ was dissolved in the mixed solution. After stirring for 10 min, 0.1 g urea was added into the above solution. Then the as-obtained solution after stirring for another 30 min was transferred into a Teflon-lined stainless steel autoclave with 50 mL capacity. The autoclave was kept in an electric oven at 180 ^oC for 24 h. After the autoclave was cooled down to room temperature, the pink products were collected, washed with distilled water and ethanol for several times, and then dried at 60 ^oC overnight.

2.3 Synthesis of porous Co_3O_4 ultrathin nanosheets

The pink $Co_2CO_3(OH)_2$ ultrathin nanosheets were calcined at 250 ^oC for 5 h in a muffle furnace. The resulting black samples were collected for further characterizations and applications.

2.4 Material characterization

The phase and crystal structure of the as-prepared samples were characterized by X-ray diffraction (XRD, a Philips X'pert PRO MPD diffractometer) with Cu-Kα radiation (λ = 0.15406 nm) in the 2θ range of 5–75° at a scanning rate of 0.05° s^{-1}. The morphologies of the products were characterized by field emission scanning

electron microscopy (FESEM, FEI Co., model Quanta-200). Transmission electron microscope (TEM), high-resolution transmission electron microscope (HRTEM) images and selected area electron diffraction images (SAED) were taken with a HRTEM analyzer (Tecnai G2 F20). Thermogravimetric analysis (TGA) and differential thermal gravity (DTG) were recorded using a thermal gravimetric analyzer (TGA-7, PE Co.) at a heating rate of temperature 10 ^{o}C/min under air flow. The surface area of the as-obtained sample was computed from the results of N_2 physisorption at 77 K (model: BECKMANSA3100 COULTER) using the BET (Brunauer-Emmett-Teller) formalism.

2.5 Electrochemical measurements

The electrochemical measurements were performed in a three-electrode cell. The working electrode was composed of porous Co_3O_4 ultrathin nanosheets (80%), acetylene black (15%) and polytetrafluoroethylene (PTFE, 5%), which was pasted onto nickel foam and dried at 60 ^{o}C for 12 h. A platinum wire electrode and a saturated calomel electrode (SCE) were used as the counter electrode and the reference electrode, respectively. Cyclic voltammetry (CV) and chronopotentiometry (CP) were tested with a CHI 660D electrochemical workstation in a 3 M KOH electrolyte.

The specific capacitance (C) of the electrode can be evaluated according to the following equation (Eq.):

$$C = \frac{I \times \Delta t}{m \times \Delta V} \qquad (1)$$

Where C (F g^{-1}) is the specific capacitance of the electrode based on the mass of active materials, I (A) is the current during discharge process, Δt (s) is the discharge time, ΔV (V) is the potential window, and m (g) is the mass of active materials.

2.6 Fabrication and measurement of gas sensors

A certain amount of the Co_3O_4 ultrathin porous nanosheets were mixed with several drops of absolute ethanol to form slurry. The slurry was coated onto a ceramic tube with a pair of Au electrodes and four Pt wires, and then dried in air. A Ni-Cr alloy filament through the tube was employed as a heater to control the operating temperature by tuning the heating voltage.

The gas sensing properties were measured using a gas sensing test system (WS-30A, Wei Sheng Electronics Technology Co., Ltd., Zhengzhou, China) at relative humidity of 50–60%. A certain amount of test object was injected onto a heating substrate and then evaporated into gas in a chamber.

The sensor sensitivity is defined as S = Rg / Ra, where Rg and Ra are the electrical resistance of the sensor in test gas and air, respectively.

3. Results and discussion

3.1. Material characterization

Figure 1a displays the XRD pattern of the precursor. It can be seen that all of the diffraction peaks can be perfectly indexed to monoclinic $Co_2CO_3(OH)_2$ (JCPDS card No. 29-1416) and no excrescent peaks are detectable. The morphology of the precursor $Co_2CO_3(OH)_2$ is sheet-like with widths of 0.5–1 μm and lengths to several micrometers, as shown in Fig. 1b. The HRTEM image (Fig. 1c) shows two sets of mutually perpendicular lattice fringes. The interplanar distances were measured to be 0.47 nm and 0.30 nm, which corresponding to the (200) and (040) planes of monoclinic $Co_2CO_3(OH)_2$, respectively. In addition, the corresponding SAED pattern further reveals the single-crystalline nature of the monoclinic $Co_2CO_3(OH)_2$ nanosheet, as shown in Fig. 1d.

The thermo-decomposition behavior of the precursor was studied by thermal-gravimetric (TG) analysis. From the TG curve in Fig. 2a, it is clear to find an apparent decomposition step. The step shows an abrupt change of the curve with a weight loss of 24.8 % at the temperature about 250 ^oC, corresponding to the theoretical analysis of 24.23 %, which indicating the oxidation of the precursor. The DTG curve reveals that decomposition temperature of $CoCO_3(OH)_2$ is about 245 ^oC. To better understand the possible phase changes and the low cost, the precursor was annealed at 250 ^oC for 5 h and then analyzed by XRD. The XRD pattern reveals that all of the peaks correspond well to cubic spinel Co_3O_4 phase (JCPDS card number 42-1467), as shown in Fig. 2b. The absence of the precursor peaks suggests that the precursor was completely transformed into Co_3O_4.

The morphology of the calcined product was studied by SEM and TEM, as shown in Fig. 3. Figure 3(a) shows that the sheet-shaped morphology is retained after

annealing, although the lengths are relatively reduced. Under a higher magnification (Fig. 3b), the thickness of the Co_3O_4 nanosheet was measured to be 20–50 nm. The TEM investigation (Fig, 3c) demonstrates that Co_3O_4 is porous structure. The HRTEM image is shown in Fig. 3d. There are two sets of lattice fringes with the interplanar distances of 0.286 nm and 0.286 nm, corresponding to the (220) and (202) planes of cubic Co_3O_4, respectively. And the intersection angle between the (220) and (202) planes is about 60°, which is according with theoretical value.

3.2. Growth mechanism

On the basis of the above experimental results and analysis, we propose a possible mechanism to explain the formation of the Co_3O_4 nanosheets. The following reactions may occur during the hydrothermal process:

$$H_2NCONH_2 + 3H_2O = 2NH_4^+ + 2OH^- + CO_2 \quad (2)$$

$$CO_2 + H_2O = CO_3^{2-} + 2H^+ \quad (3)$$

$$2Co^{2+} + 2OH^- + CO_3^{2-} = Co_2CO_3(OH)_2 \quad (4)$$

$$3Co_2CO_3(OH)_2 + O_2 = 2Co_3O_4 + 3CO_2 + 3H_2O \quad (5)$$

At the initial stage, urea can provide OH^- and CO_3^{2-} ions simultaneously during the hydrolysis [Eqs. (2–3)].[8, 28] When the reaction temperature increased to 180 ^oC, Co^{2+} ions can easily react with OH^- and CO_3^{2-} ions under hydrothermal condition and $Co_2CO_3(OH)_2$ precipitates were produced according to Eq. (4).[29] The $Co_2CO_3(OH)_2$ nuclei were formed from the precipitation reaction. Then, these nuclei began to grow and tended to aggregate to nanosheets owing to high surface energies. And it was difficult to assemble into 3D microstructures owing to the microemulsion formed by ethylene glycol in distilled water. At the second stage, $Co_2CO_3(OH)_2$ decomposed into Co_3O_4 at high temperature about 250 ^oC [Eq. (5)]. Finally, porous Co_3O_4 ultrathin nanosheets were obtained from the thermal decomposition of precursor nanosheets, accompanied by the release of CO_2 and H_2O gases during the calcination process. The detailed mechanism for the formation of porous Co_3O_4 ultrathin nanosheets is still under further investigation.

3.3. Electrochemical properties

Cyclic voltammetry (CV) curves were measured at various scan rates ranging from 10 to 100 mV s^{-1} in 3 M KOH solution to reflect the electrochemical properties of

porous Co_3O_4 ultrathin nanosheets, as shown in Fig. 4a. There are one pair redox peak in the curves, indicating that Co_3O_4 ultrathin porous nanosheets possess a typical pseudocapacitor characteristic. The corresponding redox reactions can be expressed as follows:[30, 31]

$$Co_3O_4 + OH^- + H_2O = 3CoOOH + e^- \quad (6)$$

$$CoOOH + OH^- = CoO_2 + H_2O + e^- \quad (7)$$

Galvanostatic charge–discharge curves of the Co_3O_4 ultrathin porous nanosheets are investigated at various current densities (1, 2, 3 and 4 A g^{-1}) with voltage between between –0.2 V and 0.35 V, as shown in Fig. 4b. The specific capacitances are obtained from Eq. (1). According to the results, the specific capacitances of the porous Co_3O_4 ultrathin nanosheets are 378、155、87 and 55 F g^{-1} at 1, 2, 3 and 4 A g^{-1}, respectively. In the previous research,[32, 33] the specific capacitances of the pure Co_3O_4 electrodes were only 340, 191.2 F g^{-1} at 1 A g^{-1}, respectively. The higher specific capacitance observed in our research is attributed to the porous nature of the nanosheets, which increasing the surface area of Co_3O_4 and enhancing the electrochemical activities.

For supercapacitors, cycling stability is also a very important parameter. Therefore, galvanostatic charge–discharge measurements of the porous Co_3O_4 ultrathin nanosheets for 2000 cycles are further conducted at a current density of 1 A g^{-1}, as shown in Fig. 4c. The result shows that there is a subtle decrease and the capacitance still remains about 78.5% after 2000 cycles.

Electrochemical impedance measurements were also applied for the porous Co_3O_4 ultrathin nanosheets, as shown in Fig. 4d. Clearly, the Nyquist plots before and after 2000 cycles are composed of a semicircle at the high frequency region and a straight line at the low frequency region. The semicircle in the high frequency range is attributed to the three sections: electrolyte, electroactive material and the contact resistance between the electroactive material and the current collector, and the straight line is related to the diffusive resistance. There are only slight differences between the 1st and 2000th cycles due to the block of diffusive resistance after 2000th charge–discharge.

3.4 Gas sensing measurements

The operating temperature is an important factor for semiconductor oxide sensors. Thus to select an optimum operating temperature, gas-sensing measurements were conducted with 100 ppm ethanol under various operating temperature (Fig. 5a). The sensor demonstrates that the sensitivity of the sensor increases at first and reaches the maximum, and then decreases with the operating temperature increasing. The maximum sensitivity of the sensor reaches 14.3 at 160 ^{o}C. Therefore, the temperature of 160 ^{o}C was chosen for further examining gas-sensing properties of the Co_3O_4 nanosheets, respectively.

Figure 5b shows the sensitivity of the sensor depends on the concentration of ethanol at optimum operating temperature. The sensitivity of the sensor increases with the concentration of ethanol increasing. The response increases rapidly with increasing the concentration of ethanol in the range of 10–100 ppm. Above 100 ppm, the increase of response turns slow with the ethanol concentration rising. The curve shows that the sensor could detect ethanol gas in a wide range of concentrations, starting with the minimum concentration of 10 ppm, which is below the limit (200 ppm) imposed for a breath analyser.[34] Moreover, the inset shows the nearly linear calibration curve in the range of 10–100 ppm, which indicates that the sensor is quantitatively for low concentration ethanol gas detection.[25]

To further investigate the gas selectivity property of Co_3O_4 nanosheets sensor, the sensor based on Co_3O_4 nanosheets was selected to test various gases with the concentration of 100 ppm at 160 ^{o}C, such as methanol, ethanol, formaldehyde, benzene, ammonia and acetone. As illustrated in Fig. 5c, the sensor exhibits higher sensitivity to ethanol than other gases, which demonstrates that the sensor possesses good selectivity to ethanol. The high response coupled with high sensing behavior makes it a good candidate for fabricating ethanol sensors.

In the previous research,[12, 35] the maximum sensitivities of the gas sensor based Co_3O_4 to 100 ppm ethanol were 5 and 3, respectively. We believe that the exceptional gas sensor performances in our research could be ascribed to the remarkable unique structure of Co_3O_4 nanosheets with a favorable feature.[25] In order to investigate the specific surface area and pore-size distribution of the obtained $Co_2CO_3(OH)_2$ and

Co_3O_4, Brunauer-Emmett-Teller gas-sorption measurement was performed. BET surface area of the Co_3O_4 was about 97.2 m^2 g^{-1}, as shown in Fig. 5d. From the inset of Fig. 5d, it can be seen that most of pores were around 4.7 nm in diameter and the average diameter of pores was approximately 7.8 nm. Compared to the BET surface area of precursor $Co_2CO_3(OH)_2$ (Fig. S1), the higher surface area of Co_3O_4 is attributed to the obtained porous ultrathin nanosheets structure after calcination. The high surface area and void spaces of Co_3O_4 nanosheets provide more active reaction sites between gas and active materials, which are the responsible for the fast and high response.

4. Conclusions

In summary, the porous Co_3O_4 ultrathin nanosheets were synthesized via facile hydrothermal and subsequent heat treatment methods. The CV curves of the as-prepared porous Co_3O_4 ultrathin nanosheets possessed a high specific capacitance of 378 F g^{-1} at a current density of 1 A g^{-1}. Beside the excellent electrochemical properties, the as-prepared porous Co_3O_4 ultrathin nanosheets also show good sensitivity and selectivity to ethanol as gas-sensor. All the data show that the porous Co_3O_4 ultrathin nanosheets can be suitable for electrochemical supercapacitor devices and ideal gas-sensor to ethanol.

Acknowledgements

The financial support from the Natural Science Foundation of China (No. 21301007) is acknowledged.

References

1. T. Stemmler, F. A. Westerhaus, A.-E. Surkus, M.-M. Pohl, K. Junge and M. Beller, *Green Chem.*, 2014, **16**, 4535-4540.
2. H. Sun, H. M. Ang, M. O. Tade and S. Wang, *J. Mater. Chem. A*, 2013, **1**, 14427-14442.
3. C. Yuan, L. Zhang, L. Hou, G. Pang and W.-C. Oh, *Rsc Adv.*, 2014, **4**, 14408-14413.
4. L. R. Baker, C.-M. Jiang, S. T. Kelly, J. M. Lucas, J. Vura-Weis, M. K. Gilles, A. P. Alivisatos and S. R. Leone, *Nano Lett.*, 2014, **14**, 5883-5890.
5. T. Ghosh, S. K. Dash, P. Chakraborty, A. Guha, K. Kawaguchi, S. Roy, T. Chattopadhyay and D. Das, *Rsc Adv.*, 2014, **4**, 15022-15029.
6. G.-L. Xu, J.-T. Li, L. Huang, W. Lin and S.-G. Sun, *Nano Energy*, 2013, **2**, 394-402.
7. R. B. Rakhi, W. Chen, M. N. Hedhili, D. Cha and H. N. Alshareef, *ACS Appl. Mater.*

Interfaces, 2014, **6**, 4196-4206.

8. A. K. Rai, J. Gim, T. Trang Vu, D. Ahn, S. J. Cho and J. Kim, *J. Phys. Chem. C*, 2014, **118**, 11234-11243.
9. M. Liu, S. He and W. Chen, *Nanoscale*, 2014, **6**, 11769-11776.
10. J. S. Chen, T. Zhu, Q. H. Hu, J. Gao, F. Su, S. Z. Qiao and X. W. Lou, *ACS Appl. Mater. Interfaces*, 2010, **2**, 3628-3635.
11. J. Deng, L. Wang, Z. Lou and T. Zhang, *Rsc Adv.*, 2014, **4**, 21115-21120.
12. C. Sun, X. Su, F. Xiao, C. Niu and J. Wang, *Sens. Actuators B Chem.*, 2011, **157**, 681-685.
13. T. Hu, G. Xin, H. Sun, X. Sun, M. Yu, C. Liu and J. Lian, *Rsc Adv.*, 2014, **4**, 1521-1525.
14. J. Dong, L. Song, J.-J. Yin, W. He, Y. Wu, N. Gu and Y. Zhang, *ACS Appl. Mater. Interfaces*, 2014, **6**, 1959-1970.
15. G. Bai, H. Dai, J. Deng, Y. Liu, F. Wang, Z. Zhao, W. Qiu and C. T. Au, *Applied Catalysis a-General*, 2013, **450**, 42-49.
16. G. L. Chen, C. Guyon, Z. X. Zhang, S. Ognier, J. Beem and M. Tatoulian, *Mater. Lett.*, 2013, **107**, 111-114.
17. G. A. M. Ali, O. A. Fouad and S. A. Makhlouf, *J. Alloys Compd.*, 2013, **579**, 606-611.
18. Z. Ren, Y. Guo, Z. Zhang, C. Liu and P.-X. Gao, *J. Mater. Chem. A*, 2013, **1**, 9897-9906.
19. J. Xu, P. Gao and T. S. Zhao, *Energy Environ. Sci.*, 2012, **5**, 5333-5339.
20. B. Bai, H. Arandiyan and J. Li, *Appl. Catal. B Env.*, 2013, **142**, 677-683.
21. T. Zhu, J. S. Chen and X. W. Lou, *J. Mater. Chem.*, 2010, **20**, 7015-7020.
22. M. Ma, Z. Pan, W. Wang, L. Guo, J. Li, Z. Wu and S. Yang, *J. Nanosci. Nanotechnol.*, 2013, **13**, 864-868.
23. P. Razmjoo, B. Sabour, S. Dalvand, M. Aghazadeh and M. R. Ganjali, *J. Electrochem. Soc.*, 2014, **161**, D293-D300.
24. Y. Q. Zhang, L. Li, S. J. Shi, Q. Q. Xiong, X. Y. Zhao, X. L. Wang, C. D. Gu and J. P. Tu, *J. Power Sources*, 2014, **256**, 200-205.
25. Z. Wen, L. Zhu, Y. Li, Z. Zhang and Z. Ye, *Sens. Actuators B Chem.*, 2014, **203**, 873-879.
26. D. Cai, H. Huang, D. Wang, B. Liu, L. Wang, Y. Liu, Q. Li and T. Wang, *ACS Appl. Mater. Interfaces*, 2014, **6**, 15905-15912.
27. Y. Lu, W. Zhan, Y. He, Y. Wang, X. Kong, Q. Kuang, Z. Xie and L. Zheng, *ACS Appl. Mater. Interfaces*, 2014, **6**, 4186-4195.
28. M. Roy, S. Ghosh and M. K. Naskar, *Dalton Trans.*, 2014, **43**, 10248-10257.
29. B. Wang, T. Zhu, H. B. Wu, R. Xu, J. S. Chen and X. W. Lou, *Nanoscale*, 2012, **4**, 2145-2149.
30. Y. Gao, S. Chen, D. Cao, G. Wang and J. Yin, *J. Power Sources*, 2010, **195**, 1757-1760.
31. X.-h. Xia, J.-p. Tu, Y.-j. Mai, X.-l. Wang, C.-d. Gu and X.-b. Zhao, *J. Mater. Chem.*, 2011, **21**, 9319-9325.
32. J. Deng, L. Kang, G. Bai, Y. Li, P. Li, X. Liu, Y. Yang, F. Gao and W. Liang, *Electrochim. Acta*, 2014, **132**, 127-135.
33. W. Liu, L. Xu, D. Jiang, J. Qian, Q. Liu, X. Yang and K. Wang, *CrystEngComm*, 2014, **16**, 2395-2403.
34. Z. Wen, L. Zhu, W. Mei, Y. Li, L. Hu, L. Sun, W. Wan and Z. Ye, *J. Mater. Chem. A*, 2013, **1**, 7511-7518.
35. W. Y. Li, L. N. Xu and J. Chen, *Adv. Funct. Mater.*, 2005, **15**, 851-857.

Figures Caption

Fig. 1 (a) XRD pattern; (b) SEM image; (c) HRTEM image and (d) SAED pattern form of the cobalt carbonate hydroxide nanosheets.

Fig. 2 (a)Thermogravimetric analysis (TGA) and differential thermal gravity (DTG) curves of the cobalt carbonate hydroxide nanosheets at a heating rate of temperature of 10 ^{o}C under air flow; (b) XRD pattern of the obtained Co_3O_4 nanosheets after heat treatment.

Fig.3 (a) SEM image, (b) high-magnification SEM image of porous Co_3O_4 nanosheets; (c) TEM image and (d) HRTEM image of an individual porous Co_3O_4 nanosheet.

Fig.4 (a) CV curves of Co_3O_4 at various scan rates in 3 M KOH; (b) charge–discharge curves at a series of current densities for as-obtained Co_3O_4 electrode in 3 M KOH; (c) Long-term stability curves of Co_3O_4 electrodes at a current density of 1 A g^{-1}; (d) the electrochemical impedance spectra of the electrodes at the first and 2000th cycles.

Fig. 5 (a) Sensitivities of the sensor based on porous Co_3O_4 ultrathin nanosheets (a) to 100 ppm ethanol at various operating temperatures; (b) to different ethanol concentration at optimum operating temperature of 160 ^{o}C (inset shows the linear dependence of the gas response in the range of 10–100 ppm); (c) to various gases with a concentration of 100 ppm at 160 ^{o}C; (d) BET spectra of the as-obtained porous Co_3O_4 ultrathin nanosheets; the inset shows the pore size distribution.

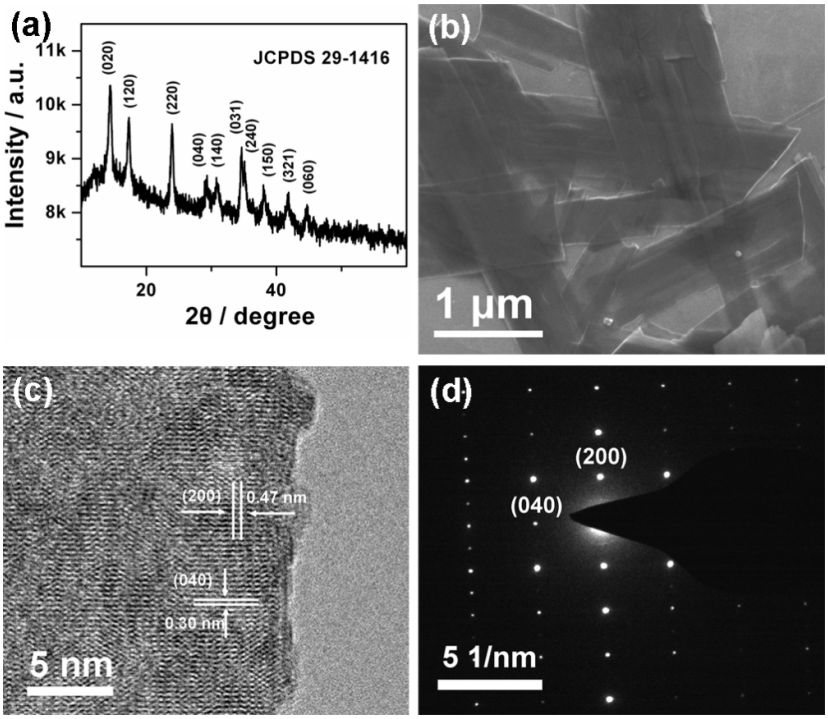

Fig. 1 (a) XRD pattern; (b) SEM image; (c) HRTEM image and (d) SAED pattern form of the cobalt carbonate hydroxide nanosheets.

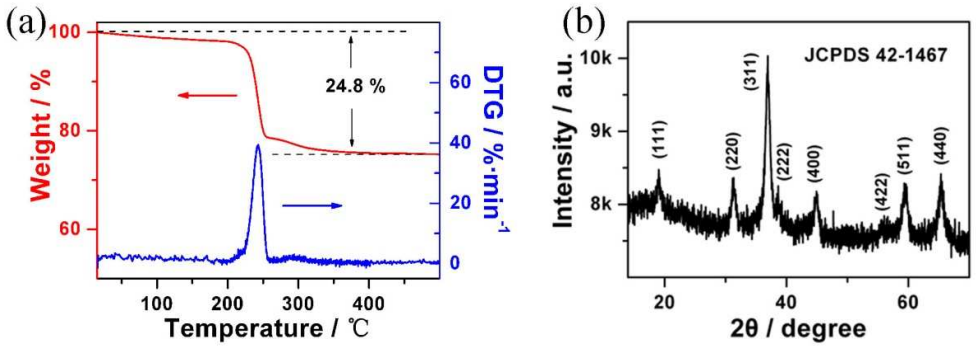

Fig. 2 (a)Thermogravimetric analysis (TGA) and differential thermal gravity (DTG) curves of the cobalt carbonate hydroxide nanosheets at a heating rate of temperature of 10 ^{o}C under air flow; (b) XRD pattern of the obtained Co_3O_4 nanosheets after heat treatment.

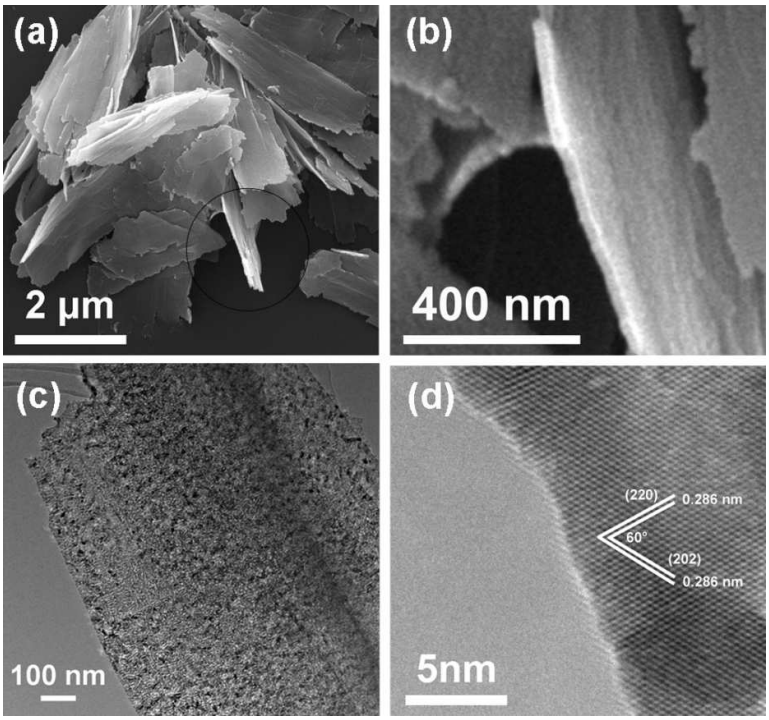

Fig.3 (a) SEM image, (b) high-magnification SEM image of porous Co_3O_4 nanosheets; (c) TEM image and (d) HRTEM image of an individual porous Co_3O_4 nanosheet.

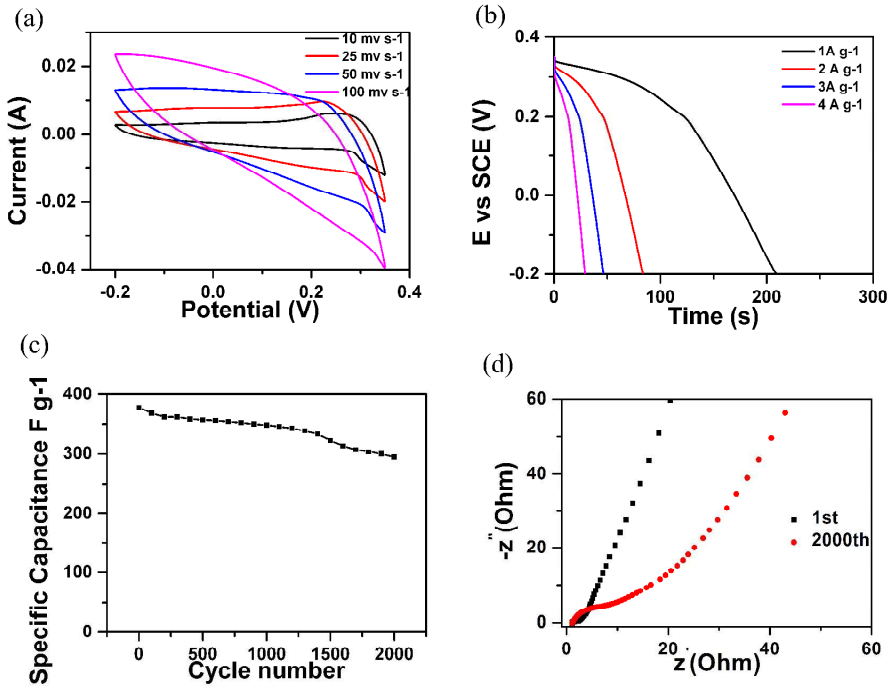

Fig.4 (a) CV curves of Co_3O_4 at various scan rates in 3 M KOH; (b) charge–discharge curves at a series of current densities for as-obtained Co_3O_4 electrode in 3 M KOH; (c) Long-term stability curves of Co_3O_4 electrodes at a current density of 1 A g^{-1}; (d) the electrochemical impedance spectra of the electrodes at the first and 2000th cycles.

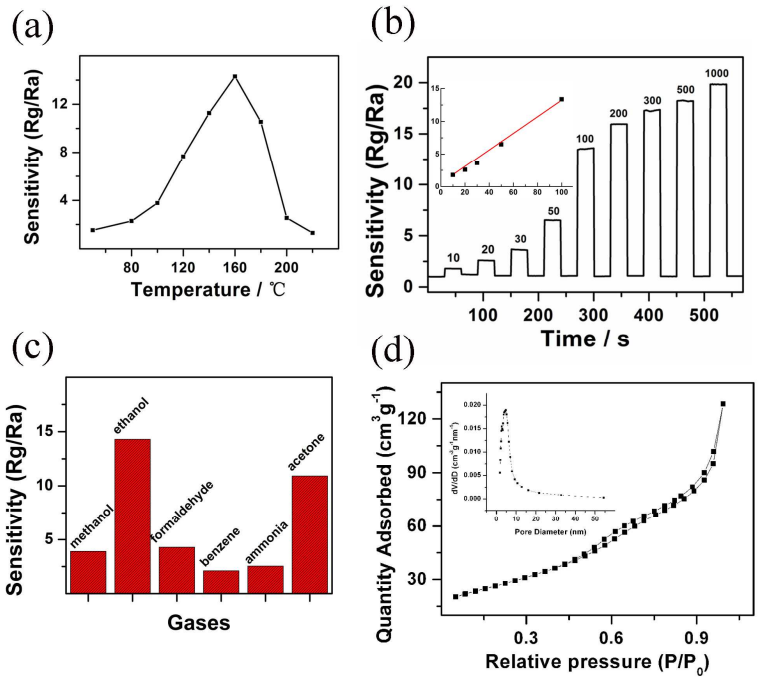

Fig. 5 (a) Sensitivities of the sensor based on porous Co_3O_4 ultrathin nanosheets (a) to 100 ppm ethanol at various operating temperatures; (b) to different ethanol concentration at optimum operating temperature of 160 ^oC (inset shows the linear dependence of the gas response in the range of 10–100 ppm); (c) to various gases with a concentration of 100 ppm at 160 ^oC; (d) BET spectra of the as-obtained porous Co_3O_4 ultrathin nanosheets; the inset shows the pore size distribution.

Graphical Abstract

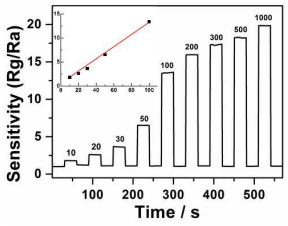

Porous Co_3O_4 ultrathin nanosheets exhibited good sensitivity and low concentration selectivity to ethanol.